J. Fluid Mech. (1996), *vol.* 307, *pp.* 167–190

Shear flow over a liquid drop adhering to a solid surface

By XIAOFAN LI AND C. POZRIKIDIS

Department of Applied Mechanics and Engineering Sciences,
University of California at San Diego, La Jolla, CA 92093-0411, USA

(Received 16 January 1995 and in revised form 5 September 1995)

The hydrostatic shape, transient deformation, and asymptotic shape of a small liquid drop with uniform surface tension adhering to a planar wall subject to an overpassing simple shear flow are studied under conditions of Stokes flow. The effects of gravity are considered to be negligible, and the contact line is assumed to have a stationary circular or elliptical shape. In the absence of shear flow, the drop assumes a hydrostatic shape with constant mean curvature. Families of hydrostatic shapes, parameterized by the drop volume and aspect ratio of the contact line, are computed using an iterative finite-difference method. The results illustrate the effect of the shape of the contact line on the distribution of the contact angle around the base, and are discussed with reference to contact-angle hysteresis and stability of stationary shapes. The transient deformation of a drop whose viscosity is equal to that of the ambient fluid, subject to a suddenly applied simple shear flow, is computed for a range of capillary numbers using a boundary-integral method that incorporates global parameterization of the interface and interfacial regriding at large deformations. Critical capillary numbers above which the drop exhibits continued deformation, or the contact angle increases beyond or decreases below the limits tolerated by contact angle hysteresis are established. It is shown that the geometry of the contact line plays an important role in the transient and asymptotic behaviour at long times, quantified in terms of the critical capillary numbers for continued elongation. Drops with elliptical contact lines are likely to dislodge or break off before drops with circular contact lines. The numerical results validate the assumptions of lubrication theory for flat drops, even in cases where the height of the drop is equal to one fifth the radius of the contact line.

1. Introduction

Liquid drops adhering to, moving along, or dislodging from solid surfaces are encountered in several natural and engineering settings and under a wide range of physical conditions. Observation of rain drops sticking to a window or moving along a windshield is a frequent experience of automobile and aircraft travellers. In aerodynamics, dislodgement of droplets due to an overpassing high-speed flow is the main mechanism for the de-wetting of aircraft surfaces (Durbin 1988*a*,*b*). In hydrodynamic cleaning, the deforming action of a shear flow is exploited for the removal of remnant droplets of a contaminant or impurity. The removal of droplets from the narrow passages of a porous medium determines the efficiency of tertiary oil recovery and plays an important role in the micromechanics of groundwater flow (Bear 1972).

In the field of cell biomechanics, liquid drops with generalized interfacial properties attached to solid surfaces are often used to model biological cells adhering to blood vessels or biomedical flow devices. Studying their behaviour in a shear flow provides us with useful information on the magnitude of the adhesion forces, and helps establish critical conditions for removal (Lipowsky, Riedel & Shi 1991).

The deformation of a drop adhering to a solid surface due to gravity or under the influence of a shear flow incorporates several fundamental aspects of flow in the presence of contact lines, and has been studied in this respect as a prototypical theoretical model (Dussan V. & Chow 1983; Dussan V. 1985, 1987). Predominant issues are the structure and stability of pendant and sessile shapes, the rearrangement of the contact lines to allow for stationary deformed shapes, and the motion of the contact lines above the critical conditions established by contact angle hysteresis.

In the absence of an external flow, a droplet adhering to a solid surface may obtain a variety of hydrostatic shapes dependent upon the geometry of the contact line. If the fluids are pure, the solid surface is perfectly smooth, and gravitational effects are weak, the distribution of the contact angle around the contact line is uniform, and the droplet obtains the shape of a section of a sphere. This shape minimizes the surface area for a given drop volume. In practice, however, interfacial contaminants and wall roughness cause the contact line to obtain arbitrary and sometimes random shapes, all of which satisfy the constraint that the contact angles lie within a certain range that is bracketed by the receding and advancing contact angles (Dussan V. 1979). The values of the latter depend upon the physical properties of the materials and roughness of the surface (Marmur 1994). Spilling water on a table and observing the shape of the developing drops demonstrate the wide variety of contact-line geometries and associated drop shapes obtained in practice. Variation of the contact angle around the contact line has been shown to be necessary in order for a drop to remain stationary on a non-horizontal surface (Milinazzo & Shinbrot 1988).

When subjected to a shear flow, a liquid drop adhering to a solid surface may exhibit two general types of behaviour. In the first case, it elongates in the principal direction of the rate-of-deformation tensor while the contact line remains stationary. When the shear rate becomes sufficiently high, the drop breaks up into two or more fragments one of which remains attached to the wall. This behaviour is similar to that of drops suspended in an infinite shear flow in the absence of a wall (Stone 1994). In the second case, which is pertinent to flat drops, the contact line rearranges itself in order to maintain the contact angle between the minimum and maximum values that are necessary for stationary deformation. At sufficiently high shear rates, the contact line begins to move causing the drop to slide. In theoretical models of the sliding motion, the velocity of the contact line normal to itself has been assumed to be proportional to a certain power of the difference between the local and the static, advancing, or receding contact angle (Haley & Miksis 1991). The shear stress at the moving contact line exhibits a singular behaviour which, however, can be either neglected or removed by introducing a finite slip velocity, with no significant consequences on overall behaviour of the drop.

Dussan V. (1987) discussed the ability of flat drops with small contact angles to stick on a solid surface in the presence of a weak shear flow, in the limit of small capillary numbers. The assumption of small contact angles allowed her to describe the motion inside the drop under the auspices of lubrication flow. Dussan V. argued that, near the critical conditions for sliding motion, the contact line obtains a composite shape that consists of two parallel straight segments along the sides and two curved sections at the upstream and downstream locations, which had been observed in

experiments (Furmidge 1962). The contact angle at the downstream section is equal to the advancing contact angle, the contact angle at the upstream section is equal to the receding contact angle, and the distribution of the contact angle along the sides ranges between these two values. Dussan V.'s asymptotic analysis applies near the critical conditions when the drop just begins to slide. In a more recent study, Feng & Basaran (1994) computed stationary finite deformations of two-dimensional air bubbles with fixed contact points protruding from a slot subject to an overpassing shear flow, using a finite-element method. Their results established critical conditions for the occurrence of steady shapes and illustrated the effects of the Reynolds and capillary numbers on the deformation of the bubbles and the streamline pattern.

In this paper we study the transient deformation of a three-dimensional liquid drop attached to a plane wall with a specified contact line subject to a suddenly applied simple shear flow. In the first part of the investigation we compute and discuss families of hydrostatic shapes in the absence of shear flow, parameterized by the drop volume and shape of the contact line. Specifying the contact line renders the distribution of contact angle an unknown that emerges as part of the numerical solution. We consider, in particular, contact lines with circular and elliptical shapes with aspect ratios up to 4. The study of these shapes is motivated by a physical scenario in which the contact line of a drop rearranges itself under the action of a shear flow so that the distribution of the contact angle falls within the range required to prevent sliding; the elliptical shapes are approximations of the composite shape observed experimentally and adopted by Dussan V. in her analysis of flat drops at small capillary numbers near the critical conditions for sliding motion.

In the second part of the investigation we consider transient motions and asymptotic behaviour in a suddenly applied shear flow, examining the effects of drop volume, shape of the contact line, and capillary number. To render the computational cost affordable, we assume that the viscosity of the drop is equal to that of the ambient fluid. The parameters of the initial-value problem are the drop volume, shape and the contact line, and capillary number. The numerical results allow us to establish conditions for steady deformation, continued elongation, or sliding motion along the wall, explained on the basis of contact-angle hysteresis.

Computing transient motions up to a steady shape is an alternative to computing steady shapes using an iterative numerical method (Feng & Basaran 1994): one disadvantage of the transient method is increased computational cost; two advantages are straightforward surface parameterization and a direct correspondence with physical experimentation. Both methods provide information on the stability of steady shapes, the transient method by monitoring the physical motion at long times, and the direct method by monitoring the properties of the iterative algorithm used to compute the steady shapes.

The numerical study of hydrostatic shapes is based on a finite-difference solution of the Young–Laplace equation written in terms of surface curvilinear coordinates. The numerical studies of the Stokes flow problem are conducted using the standard boundary-integral method; the numerical implementation incorporates a high-order method of computing the mean interfacial curvature, and an adaptive global parameterization of the interface that maintains a high degree of spatial resolution at large deformations. Both of these features are necessary for an accurate computation of the motion at large deformations.

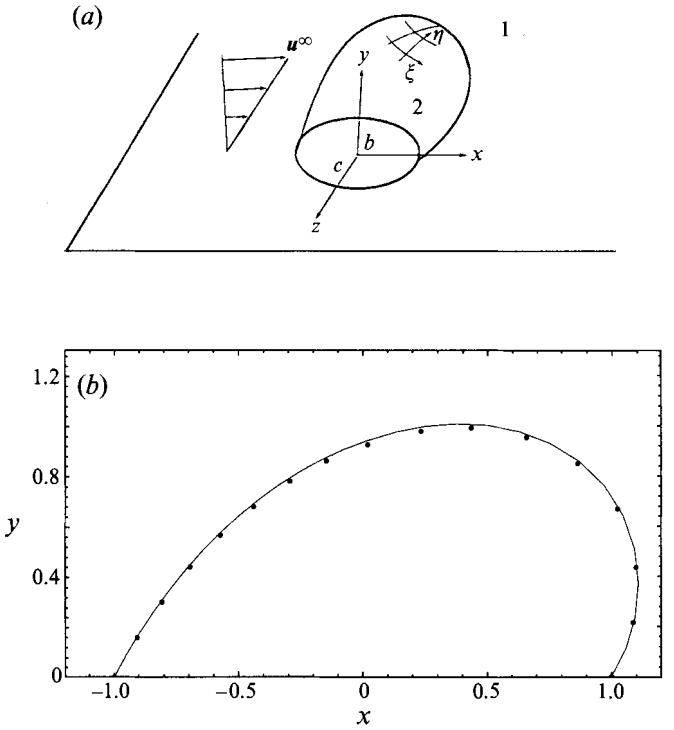

FIGURE 1. (*a*) Schematic illustration of a three-dimensional drop adhering to a planar solid surface located at $y = 0$, subject to a semi-infinite simple shear flow u^∞. The contact line has an elliptical shape with major and minor axes respectively equal to $2b$ and $2c$. (*b*) Comparison of deformed drop contours in the (x, y)-plane at steady state for the conditions described in the caption of figure 6(*c*) with a coarse and a fine grid: solid line, 24×12 initial grid; dots, 12×6 initial grid.

2. Mathematical formulation and numerical method

Consider a liquid drop of volume V resting on a plane wall below a semi-infinite body of another fluid as depicted in figure 1(*a*); the wall is located at $y = 0$. The interface between the drop and the ambient fluid exhibits uniform surface tension γ, and the contact line is required to have a certain specified shape. When the volume of the drop is sufficiently small, the effects of gravity may be neglected, and the wall may be considered to be inclined at an arbitrary angle with respect to the horizontal direction. We want to compute the hydrostatic shape of the drop in the absence of flow, and its transient and asymptotic deformation under the action of a suddenly applied simple shear flow along the x-axis as shown in figure 1(*a*). The viscosities of the fluids play no role in the hydrostatic state, but affect the structure of the flow and deformation of the interface during the unsteady and asymptotic motion. Computational constraints to be discussed later in this section require that we restrict our attention to instances where viscosity of the drop μ is equal to that of the ambient fluid.

2.1. *Computation of hydrostatic shapes*

When the ambient fluid is quiescent, and in the absence of significant gravitational effects, the drop assumes a hydrostatic shape with constant mean curvature κ_m that is independent of the physical properties of the fluids. For instance, when the contact line is a circle of a certain radius b, the interface assumes the shape of a section of

a sphere with centre at $(0, -b\tan\alpha, 0)$ and radius $R = b\sec\alpha$, where α satisfies the relation $V = \pi(8 - 9\sin\alpha - \sin 3\alpha)R^3/12$.

To compute the shape of a stationary drop with an arbitrary contact line, we describe the interface in terms of two surface curvilinear coordinates ξ and η as shown in figure 1(*a*), and compute the Cartesian coordinates of interfacial grid points so as to satisfy the condition of constant mean curvature with invariant volume constraint

$$\left.\begin{array}{lcll} \kappa_m - \kappa_0 & = & 0, & \text{at each grid point,} \\ V - V_0 & = & 0, & \end{array}\right\} \tag{2.1}$$

where κ_0 and V_0 are two constants. The mean curvature is computed according to the formula

$$\kappa_m = \frac{1}{2}\frac{\left(\dfrac{\partial \boldsymbol{x}}{\partial\eta}\cdot\dfrac{\partial \boldsymbol{x}}{\partial\eta}\right)\left(\dfrac{\partial^2 \boldsymbol{x}}{\partial^2\xi}\cdot\boldsymbol{n}\right) - 2\left(\dfrac{\partial \boldsymbol{x}}{\partial\xi}\cdot\dfrac{\partial \boldsymbol{x}}{\partial\eta}\right)\left(\dfrac{\partial^2 \boldsymbol{x}}{\partial\xi\partial\eta}\cdot\boldsymbol{n}\right) + \left(\dfrac{\partial \boldsymbol{x}}{\partial\xi}\cdot\dfrac{\partial \boldsymbol{x}}{\partial\xi}\right)\left(\dfrac{\partial^2 \boldsymbol{x}}{\partial^2\eta}\cdot\boldsymbol{n}\right)}{\left(\dfrac{\partial \boldsymbol{x}}{\partial\xi}\cdot\dfrac{\partial \boldsymbol{x}}{\partial\xi}\right)\left(\dfrac{\partial \boldsymbol{x}}{\partial\eta}\cdot\dfrac{\partial \boldsymbol{x}}{\partial\eta}\right) - \left(\dfrac{\partial \boldsymbol{x}}{\partial\xi}\cdot\dfrac{\partial \boldsymbol{x}}{\partial\eta}\right)^2}, \tag{2.2}$$

where $\boldsymbol{n}$ is the unit vector normal to the interface pointing into the ambient fluid (Pozrikidis 1995*b*, Chapter 1).

Considering interfaces with four-fold azimuthal symmetry as shown in figure 3(*a*), we divide the axis of the drop from the origin up to the point of maximum elevation $y = d$ into N intervals $y_i/d = t_i, i = 1, N$, where the ascending sequence of dimensionless ratios $\{t_i\}$ take values between zero and unity. To compute t_i we assume that the trace of the interface in the (x, y)-plane is part of a circle: $\{t_i\}$ corresponds to evenly spaced divisions of the polar angle in the (x, y)-plane. The constant-η lines are restricted to lie in planes that are perpendicular to the y-axis at $y = y_i$. The constant-ξ lines lie in M azimuthal planes that are evenly distributed with respect to the azimuthal angle φ. Having specified the volume V_0 and the geometry of the contact line, the unknowns are the polar cylindrical radial distance σ of the grid points from the y-axis, the maximum elevation d, and the constant mean curvature κ_0.

Enforcing equations (2.1) and approximating the partial derivatives with finite differences provides us with a system of $(N-1)M + 2$ nonlinear algebraic equations for the unknowns. The first and second derivatives in (2.2) are computed using the five-point Lagrange's formula (Abramowitz & Stegun 1970, Chapter 25), with associated truncation error in the mean curvature of $O(N^{-3})$ or $O(M^{-3})$. The system of nonlinear equations is solved using Newton's method with the Jacobian matrix computed at each iteration by numerical differentiation. Under most circumstances, the convergence of the method is quadratic, as expected. When the interface tends to become tangential to the wall around the base, however, the aforementioned surface parameterization becomes inappropriate, and this results in slow convergence or even divergence of the iterative method. Fortunately, this pathology occurs only for contact lines with high aspect ratios as described in the next section. To this end, it is worth noting that the present numerical method is an alternative to methods based on variational principles for the free energy of the interface developed by previous authors (see, for example, Milinazzo & Shinbrot 1988; Hornung & Mittelmann 1990).

The implementation of the numerical method with a 16×16 grid over a quarter of the drop runs for 2–5 minutes on a SUN SPARCstation 1 workstation to achieve

third-decimal-place accuracy in the mean curvature. The precise amount of required CPU time depends upon the geometry of the contact line and drop size.

2.2. *Computation of evolving shapes*

To compute the deformation of a drop in simple shear flow, we adopt the standard boundary integral formulation. Under the stipulation that the viscosity of the drop is equal to that of the ambient fluid, we obtain an integral representation for the velocity at a point $\boldsymbol{x}_0$ that is located inside the drop, outside the drop, or at the interface, in terms of the incident velocity and a single-layer potential due to the discontinuity in the traction across the interface $\Delta\boldsymbol{f}$,

$$u_j(\boldsymbol{x}_0) = u_j^{\infty}(\boldsymbol{x}_0) - \frac{1}{8\pi\mu}\int_{S_D} \Delta f_i(\boldsymbol{x}) G_{ij}^{W}(\boldsymbol{x}, \boldsymbol{x}_0)\, \mathrm{d}S(\boldsymbol{x}), \tag{2.3}$$

where

$$\boldsymbol{u}^{\infty}(\boldsymbol{x}_0) = (ky_0, 0, 0), \quad \Delta\boldsymbol{f} = 2\gamma\kappa_m\boldsymbol{n}. \tag{2.4}$$

The kernel $\mathbf{G}^W$ is the Green's function of Stokes flow bounded by an infinite plane wall discussed by Pozrikidis (1992). Note that the assumption of equal viscosities has allowed us to obtain the integration representation (2.3) instead of a Fredholm integral equation for the interfacial velocity, which would be the case if the viscosity ratio had any value between zero and infinity except unity.

The deformation of the drop is described by marking the interface with a grid of marker points $\boldsymbol{x}_{ij}$, and then advancing the position of the marker points according to the velocity of the fluid, which is equal to the right-hand side of (2.3). To prevent clustering of the marker points due to the shearing motion, we advance their position with the velocity of the fluid normal to the interface, according to the equation

$$\frac{\mathrm{d}\boldsymbol{x}_{ij}}{\mathrm{d}t} = (\boldsymbol{u}(\boldsymbol{x}_{ij}) \cdot \boldsymbol{n}(\boldsymbol{x}_{ij}))\boldsymbol{n}(\boldsymbol{x}_{ij}). \tag{2.5}$$

In the numerical implementation of the method, we take advantage of the fore-and-aft symmetry of the flow with respect to the (x, y)-plane to reduce the computational domain to half the surface of the drop, and describe the interface in terms of the two surface curvilinear coordinates ξ and η shown in figure 1(*a*). The marker points are located at the intersections of the ξ- and η-lines, which at the initial instant are distributed evenly with respect to arclength in their respective directions; their position is computed by interpolating from the hydrostatic shape.

2.2.1. *Evaluation of the single-layer integral*

The single-layer integral in equation (2.3) over the drop interface S_D, denoted by SLI, is approximated with the sum of integrals over the boundary elements $\{E_n\}$, which are planar triangles connecting three neighbouring marker points and triangulating the whole interface,

$$\mathrm{SLI} \approx -\frac{\gamma}{4\pi\mu}\sum_{E_n}\int_{E_n} \kappa_m(\boldsymbol{x}) n_i(\boldsymbol{x}) G_{ij}^{W}(\boldsymbol{x}, \boldsymbol{x}_0)\, \mathrm{d}S(\boldsymbol{x}). \tag{2.6}$$

The Green's function $\mathbf{G}^W(\boldsymbol{x}, \boldsymbol{x}_0)$ exhibits a singular behaviour as $1/r$ as $r \equiv |\boldsymbol{x}-\boldsymbol{x}_0| \to 0$, which is removed by replacing $\kappa_m(\boldsymbol{x})$ in (2.6) with $(\kappa_m(\boldsymbol{x}) - \kappa_m(\boldsymbol{x}_0))$. Conservation of mass for the flow due to a point force guarantees that this modification does not alter the value of the single-layer integral. The remaining non-singular integrand shows a discontinuous behaviour at the point $\boldsymbol{x}_0$, accompanied by substantial oscillations.

As a result, the accuracy of the SLI is limited by the computation of the integrals over the elements that are adjacent to the singular point $\boldsymbol{x}_0$. To address this issue, we classify the boundary elements $\{E_n\}$ into two sets. One set contains the triangles with one node at the singular point $\boldsymbol{x}_0$, and the second set contains the so-called regular triangles. To compute the integral over the first set of triangles, we express the integration variables in local polar coordinates with origin at $\boldsymbol{x}_0$ and then use the four-point Gauss–Legendre quadrature for integration in the radial and polar angular directions (Pozrikidis 1995*a*). The mean curvature at the grid points is computed as described in § 2.1 for the hydrostatic case, using formula (2.2). The values of κ_m and $\boldsymbol{n}$ at the quadrature points over the triangular elements are obtained using bilinear interpolation with respect to the curvilinear coordinates. To compute the integral over the regular triangles we use the three-point Gaussian quadrature over a triangular domain (see for example Zienkiewicz & Taylor 1989, p.176).

It is worth noting that an alternative method of computing the SLI that circumvents the explicit computation of the mean curvature described in Pozrikidis (1993,1995*a*), did not produce consistently accurate results. Although it was successful for drop shapes whose mean curvature has a uniform sign, it caused numerical instabilities when the drops obtained convoluted shapes with convex and concave profiles and directional normal curvatures with positive and negative sign.

After the velocity at the marker points has been computed, their position is advanced using the fifth-order embedded Runge–Kutta method (Press *et al.* 1992, p.717). The high-order adaptive time-stepping method becomes necessary when the drop reaches a nearly stationary shape, and when the mesh points move close to each other due to large interfacial deformations. The latter is evident, for instance, in figure 7, which is discussed in § 4.

2.2.2. *Regriding and numerical accuracy*

As the drop elongates under the influence of the incident shear flow, regriding and mesh refinement become necessary in order to maintain an acceptable level of accuracy and spatial resolution. In the numerical procedure, we examine the distribution of marker points after each time step with two objectives. When the arclength of one of the ξ-lines around the drop exceeds a given threshold, we increase the number of η-lines M by one unit, and reposition the grid points using cubic spline interpolations along each ξ-line, so that the ξ-lines become evenly distributed with respect to arclength. Similarly, when the total arclength of one of the η-lines exceeds a preset maximum length, we add one ξ-line using this method. Thirdly, when the spacing between two consecutive ξ or η grid lines becomes larger than a certain given threshold, we reposition all grid points using cubic spline interpolation along each η- or ξ-line to achieve even spacing in arclength.

To examine the accuracy of the numerical method, we compare numerical results with identical initial and boundary conditions, stated in the caption of figure 6(*c*), conducted using a coarse 12×6 and a finer 24×12 grid over half the interface. In both computations, the drop reaches a stationary shape after a finite evolution period, at which point the grid sizes have increased, respectively, to 12×8 and 24×14 due to mesh refinement. In figure 1(*b*) we indicate with dots and plot with a solid line the cross-sections of the drop in the (x, y)-plane at steady state and observe small differences within the order of the numerical error due to the finite mesh size.

The computations discussed in §§ 4 and 5 are carried out starting with either a 16×8 grid or a 20×16 grid, depending upon the geometrical complexity of the initial drop shape. In all cases, the cumulative change in the drop volume due to numerical

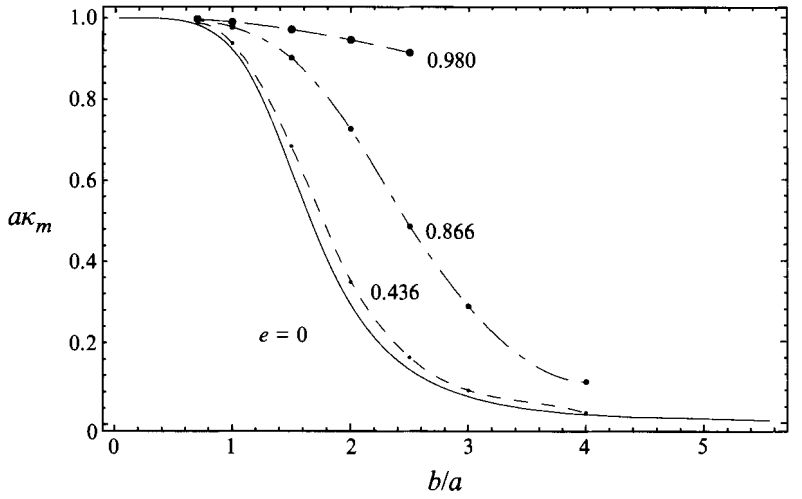

FIGURE 2. Graphs of the reduced mean curvature $a\kappa_m$ as a function of the reduced major dimension of the base contact line b/a, where a is the equivalent drop radius, for eccentricities $e = 0, 0.436, 0.866, 0.980$ constructed from the numerical results. The dots represent the numerical data.

error was less than 1% of the initial value from the beginning to the end of the computation. A complete run in each case takes from 0.1 hr to 2 hr of CPU time on the Cray C90 computer of the San Diego Supercomputer Center with optimized compilation.

3. Hydrostatic shapes

In the numerical studies we consider drops whose contact lines have elliptical shapes with semi-axes in the x- and z-directions respectively equal to b and c as shown in figure 1(a). Non-dimensionalizing all lengths by the equivalent drop radius a, defined in terms of the volume of the drop V as $a = (V/(4\pi/3))^{1/3}$, we find that the hydrostatic shape of a drop depends upon the size and aspect ratio of the contact line expressed by the two geometrical ratios b/a and c/a. Because of the four-fold symmetry of the interfaces, it suffices to consider shapes with $b \geqslant c$, where the major axis of the contact line is oriented along the x-axis. Furthermore, it is convenient to introduce the eccentricity of the contact line $e = (1-(c/b)^2)^{1/2}$ and discuss the shapes in terms of b/a and e. As e increases from zero to unity, the contact line reduces from a circle, to an elongated ellipse, to a straight segment.

The mean curvature of a drop with a circular contact line, corresponding to $e = 0$, is computed readily in closed form using simple geometrical arguments, and is found to be given by $b\kappa_m = \cos\beta$, where β is determined from the equation $\sin 3\beta + 9\sin\beta - 8 + 16(a/b)^3\cos^3\beta = 0$. A graph of $a\kappa_m$ against b/a yields the solid line shown in figure 2. As b/a tends to zero, the interface tends to become a whole sphere, and the mean radius of curvature tends to become equal to the equivalent radius yielding $a\kappa_m = 1$. On the other hand, as b/a tends to infinity, the interface assumes the shape of an increasingly smaller section of a sphere, and the mean radius of curvature becomes much larger than the equivalent radius yielding $a\kappa_m = 0$.

Numerical results for finite contact-line eccentricities show a similar behaviour, as illustrated in figure 2 for $e = 0.436, 0.866, 0.980$ corresponding to aspect ratios

$e \backslash b/a$	0.7	1.0	1.5	2.0	2.5	3.0	4.0
0	0.983	0.920	0.621	0.292	0.131	0.065	0.021
0.436	0.986	0.936	0.681	0.346	0.161	0.080	0.026
0.866	0.994	0.977	0.897	0.723	0.484	0.287	0.101
0.980	0.997	0.989	0.968	0.942	0.910		

TABLE 1. Dimensionless mean curvature $a\kappa_m$ of different eccentricities

$c/b = 0.9, 0.5, 0.2$. The precise values of $a\kappa_m$ for a range of values of b/a are collected in table 1. Accurate results for high eccentricities were prohibited by the occurrence of convoluted interfacial shapes at small volumes requiring a different type of interfacial parameterization as discussed in §2. As the size of the contact line is reduced, the interfaces tend to obtain the shape of a whole sphere, and the radius of curvature tends to become equal to the equivalent radius a irrespectively of the aspect ratio. This occurrence reveals the physically intuitive behaviour that the precise shape of a small contact line has a small influence on the spherical shape of a larger drop. As b/a becomes large, the interfaces tend to obtain an asymptotic shape whose precise form depends upon the aspect ratio of the contact line. The y-coordinate of the interface in this limit, which can be regarded as the height of the interface, satisfies Poisson's equation with a constant forcing term that is proportional to twice the mean curvature, and is subject to homogeneous Dirichlet boundary conditions around the contact line (Pozrikidis 1995*b*, Chapter 4). A plot of the height of the interface as a function of x and z yields the velocity distribution for pressure-driven flow in a tube whose contour coincides with the contact line. Figure 2 shows that the curvature of the interface in this limit tends to vanish independently of the aspect ratio of the contact line.

The reduced mean curvature $a\kappa_m$ is a measure of the deviation of the main body of the drop from the spherical shape. For a certain value of the geometrical ratio b/a, there is a transitional value of the eccentricity below which the interface is nearly spherical and above which it obtains a more involved shape and finally tends to obtain an asymptotic flattened shape. In figure 3(*a–c*) we present a sequence of shapes for $b/a = 2^{1/3} \approx 1.26$ and $e = 0.436, 0.866, 0.980$ corresponding to $c/b = 0.9, 0.5, 0.2$. The eccentricity of the contact line for $e = 0.436$ is sufficiently small so that the interface takes the shape of a nearly perfect hemisphere. Higher eccentricities yield more convoluted shapes especially around the base. The changes in the interfacial shape with varying the eccentricity are better illustrated by plotting cross-sections of the interfaces in the (x,y)- and (y,z)-planes, shown in figure 3(*d*, *e*). It is interesting to note that as e is increased, the interface tends to form a skirt around the base in the (x,y)-plane, and obtains a nearly cylindrical shape in the (y,z)-plane.

Similar behaviour is observed for larger drops with $b/a = 0.7$ depicted in figure 4(*a–e*). A noteworthy difference is that the skirting of the interface in the (x,y)-plane near the contact line is masked by a global retraction of the main body of the drop yielding a slight dimple around the base as shown in figure 4(*d*). Corresponding results for smaller drops with $b/a = 2.0$ are shown in figure 5(*a–e*). The skirting around the base in the (x,y)-plane is pronounced, and the transition to highly elongated asymptotic shapes is evident at high eccentricities.

A circular contact line has a uniform contact angle given by $\Theta = \pi/2 - \alpha$ where α was defined in the first paragraph of §2.1. In figures 3(*f*), 4(*f*) and 5(*f*) we plot the distribution of Θ as a function of the azimuthal angle φ measured around the y-axis

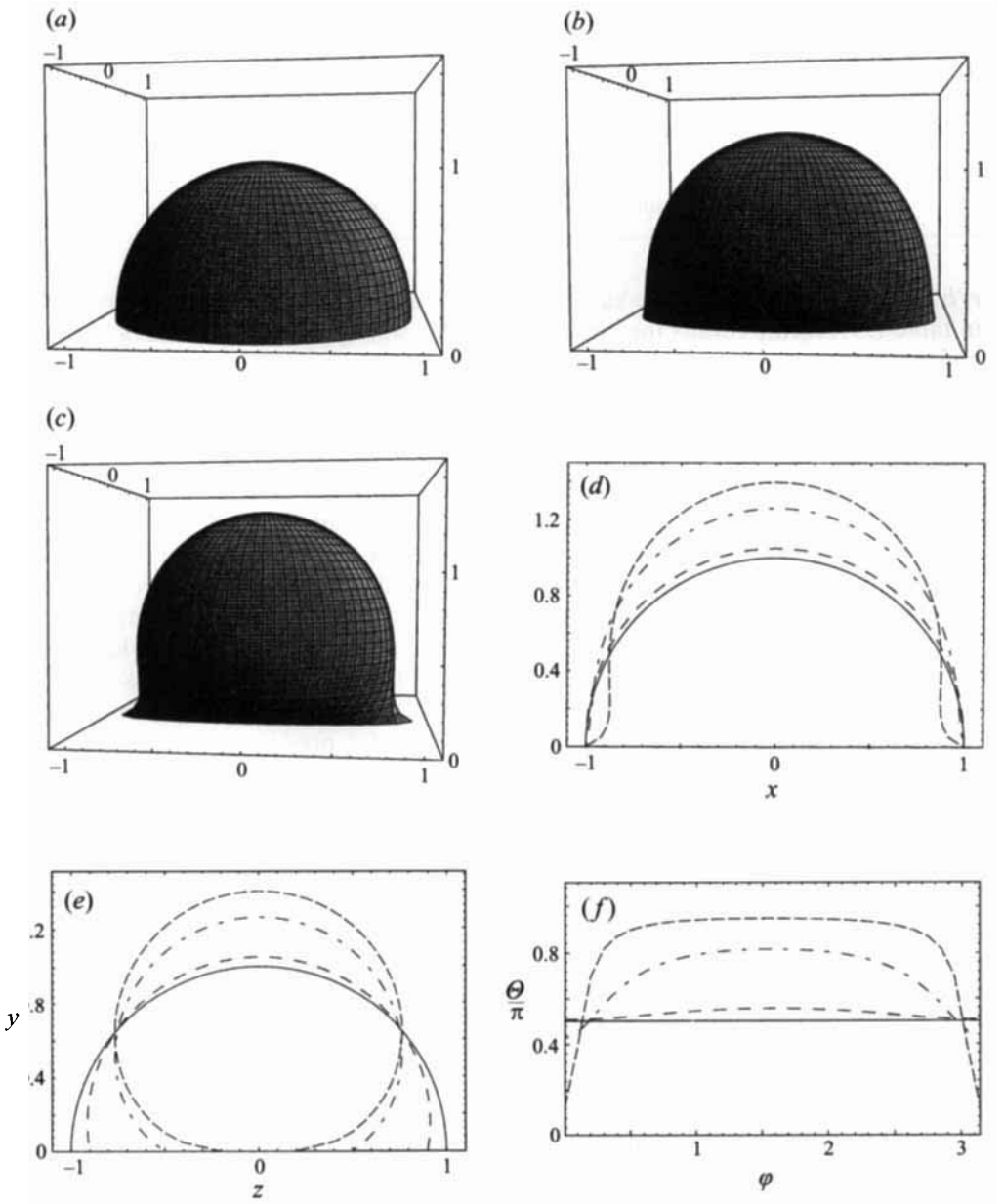

FIGURE 3. Hydrostatic drop shapes with $b/a = 1.26$ and various contact-line eccentricities; when the contact line is a circle, the shape of the drop is a hemisphere. (*a–c*) An elliptical contact line with eccentricity (*a*) $e = 0.436$; (*b*) $e = 0.866$; (*c*) $e = 0.980$. (*d,e*) Cross-sections of the interfaces in (*d*) the (x, y)-plane and (*e*) the (y,z)-plane: ——, $e = 0$; – – –, $e = 0.436$; – · –, $e = 0.866$; ———, $e = 0.980$. (*f*) The contact angle Θ/π plotted as a function of the azimuthal angle φ; line styles as in (*d, e*).

from the negative part of the x-axis, for several values of the contact-line eccentricity. In all cases we observe that minimum and maximum contact angles, Θ_{min} and Θ_{max}, occur, respectively, in the $z = 0$ and $x = 0$ planes. The variations are mild for aspect ratios up to 2, but become pronounced for more elongated shapes. It is interesting to note, in particular, that the contact angle for $e = 0.980$ shown in figure 5(f) is close

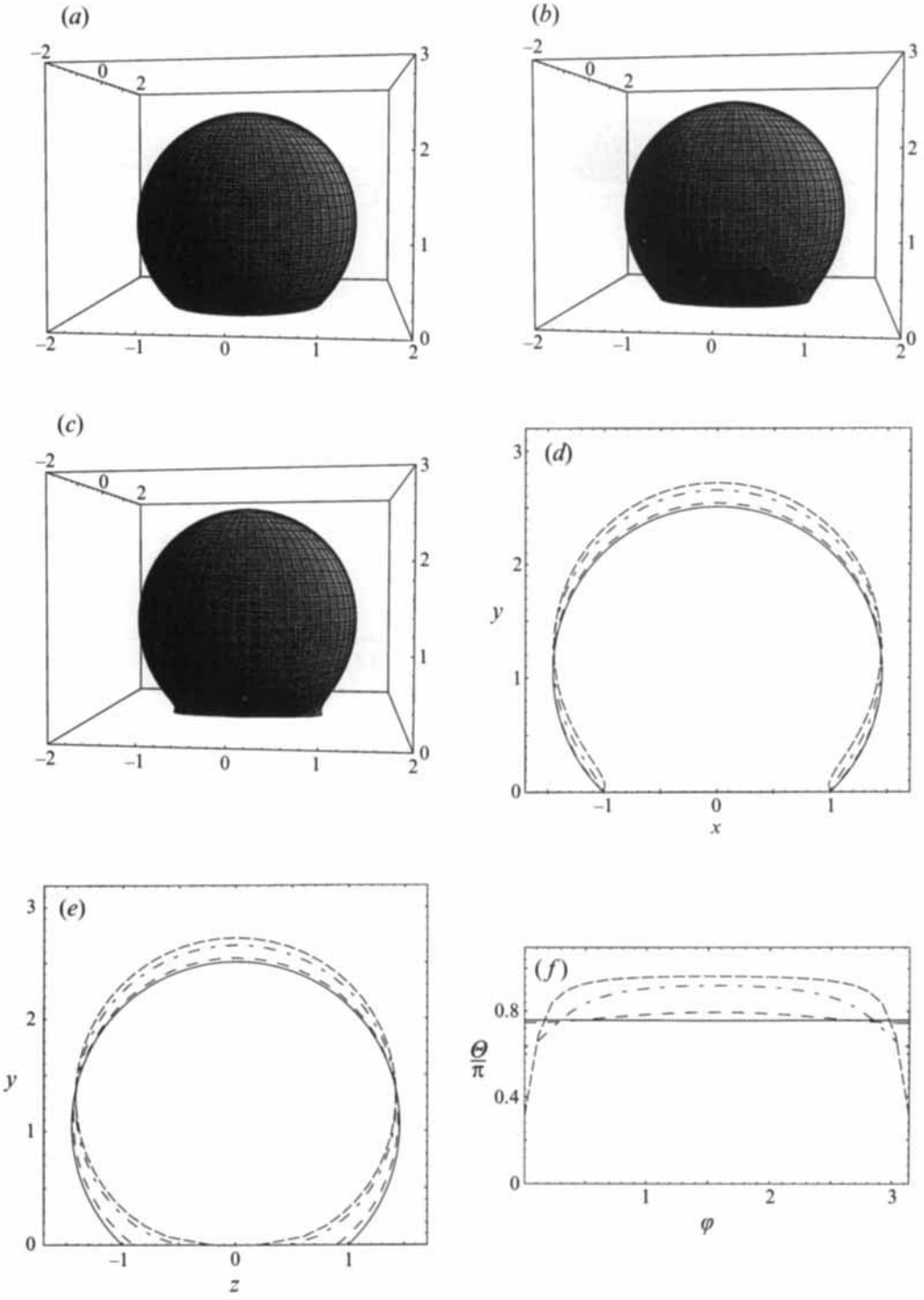

FIGURE 4. Same as figure 3 but for $b/a = 0.7$.

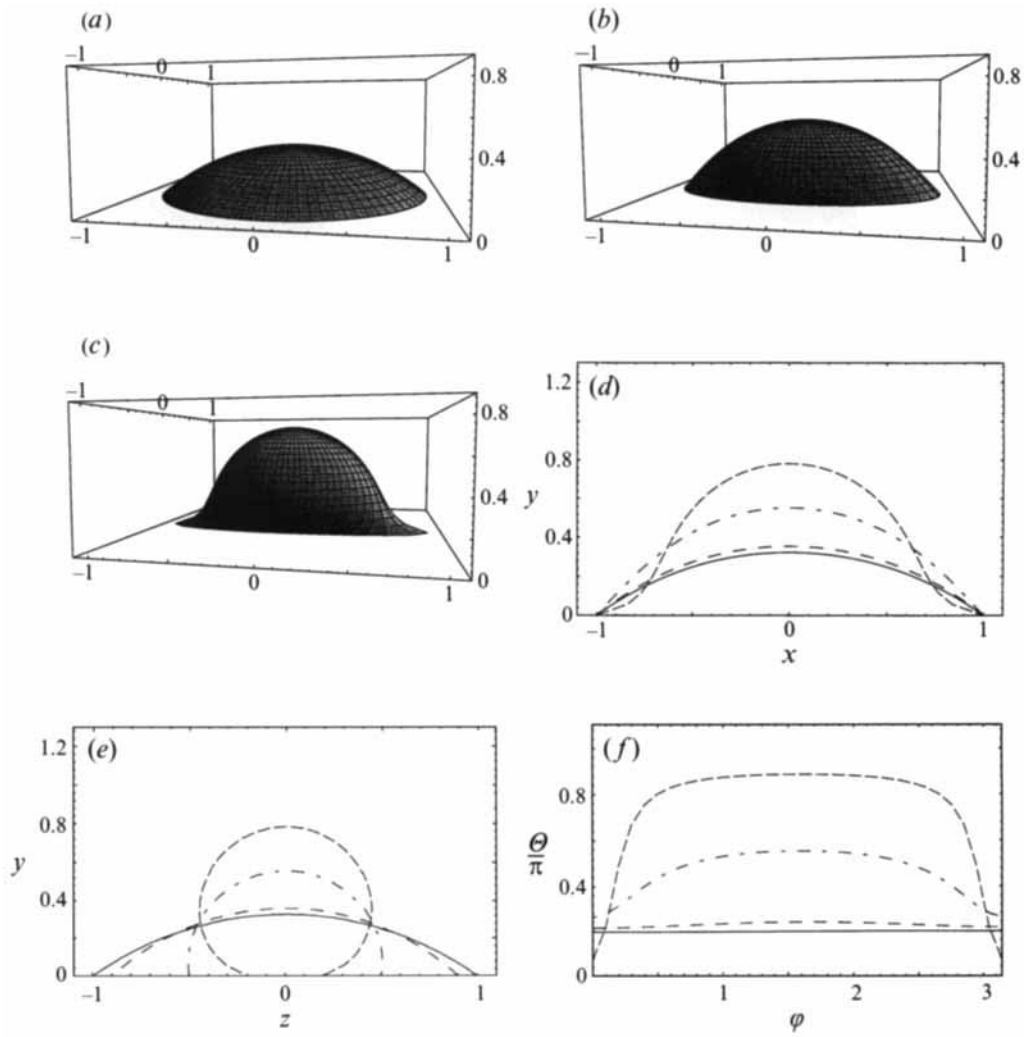

FIGURE 5. Same as figure 3 but for $b/a = 2$.

to zero at the major axis, which means that the interface is nearly tangential to the wall.

In practice, the contact line will remain stationary and the drop will be static as long as the contact angle, Θ, is less than the advancing contact angle Θ_A but higher than the receding contact angle Θ_R, $\Theta_R < \Theta < \Theta_A$; Θ_A and Θ_R are physical constants dependent upon the physical properties of the fluids and wall roughness (Dussan V. 1979). Having specified these constants, one may use figures 3(f), 4(f), 5(f) to predict the critical aspect ratio of the contact line above which stationary drop shapes cannot be established.

4. Deformation of drops with circular contact lines

Non-dimensionalizing all variables using as length scale the equivalent drop radius a and time scale the inverse shear rate $1/k$, we find that the transient motion and asymptotic deformation of a drop with a circular contact line in a suddenly applied

simple shear flow depends upon the reduced radius of the contact line $b/a = c/a$ and capillary number defined as $Ca = \mu k h/\gamma$ where h is the maximum height of the drop in the hydrostatic state. The choice of this length scale emerges by balancing the magnitudes of the deforming viscous stresses and of the restraining stresses due to the capillary pressure over the interface. Two central objectives of the computations are to describe the magnitude of the drop deformation, and identify changes in the distribution of the contact angle around the contact line as a result of the motion.

4.1. *Hemispherical drop*

First, we consider the deformation of a drop with a hemispherical hydrostatic shape corresponding to $a/b = a/c = 0.794$, and examine the motion as a function of the capillary number. In figure 6(a, b), we plot with solid lines the maximum magnitude of the component of the velocity normal to the interface, $\|\boldsymbol{u}\cdot\boldsymbol{n}\|_\infty = \max_{\boldsymbol{x}\in S_p} |\boldsymbol{u}(\boldsymbol{x})\cdot\boldsymbol{n}(\boldsymbol{x})|$, and the deformation parameter $D = (A - B)/(A + B)$ as functions of time since the beginning of the motion for $Ca = 0.126$. A and B are, respectively, the maximum and minimum radial distances of the interface from the origin of the global coordinate system in the (x,y)-plane. Figure 6(a) shows that the magnitude of the normal component of the velocity decays exponentially in time as $\|\boldsymbol{u}\cdot\boldsymbol{n}\|_\infty \sim \mathrm{e}^{-\delta t}$, with a decay constant δ that is approximately equal to $2.06k$. Figure 6(b) shows that the deformation parameter D approaches an asymptotic value that is approximately equal to 0.21. Consequently, the drop deforms and then reaches the steady shape shown in figure 6(c), where the deforming viscous stresses are balanced by the capillary pressure. The asymptotic inclination of the maximum radial distance in the (x,y)-plane with respect to the x-axis is equal to 0.206π. As a secondary point pertaining to the performance of the numerical method, we note that the singular point of the surface coordinate system remains at the top of the drop during the deformation. The fact that the surface coordinate lines are smooth and remain dense guarantees that the computations are carried out with accuracy and adequate spatial resolution.

4.1.1. *Effect of capillary number on deformation*

The numerical results show that as Ca is increased, the drop takes an increasingly more deformed asymptotic shape. In figure 6(d) we plot cross-sections of steadily deformed drops in the (x, y)-plane for $Ca = 0.063, 0.126, 0.157$ and 0.22. The asymptotic shapes are qualitatively similar to the steady shapes of two-dimensional inviscid bubbles emerging from a slot computed by Feng & Basaran (1994) and shown in their figure 5.

To illustrate the relationship between the capillary number and asymptotic deformation in quantitative terms, in figure 6(e) we plot with dots the deformation parameter D at steady state as a function of Ca, and observe a monotonic increase. At small deformations the curve $D(Ca)$ is linear with a slope that is approximately equal to 1.55. Noting that the corresponding slope for a spherical drop suspended in an *infinite* simple shear flow is equal to $35/32 \approx 1.09$ (Taylor 1932) suggests that the presence of the wall promotes the deformation of the drop, by accentuating the magnitude of the deforming viscous stresses. Additional supportive evidence for the deformation action of the wall is provided by the observations that (a) the shear stress at the top of a rigid hemispherical protrusion on a plane wall due to an overpassing simple shear flow is higher than that at the top of a solid spherical particle that is suspended in an infinite simple shear flow by a small factor of 1.012 (Pozrikidis 1995c), and (b) the presence of a wall exacerbates the deformation of a nearby spherical drop in shear flow (Kennedy, Pozrikidis & Skalak 1994). The numerical results show that,

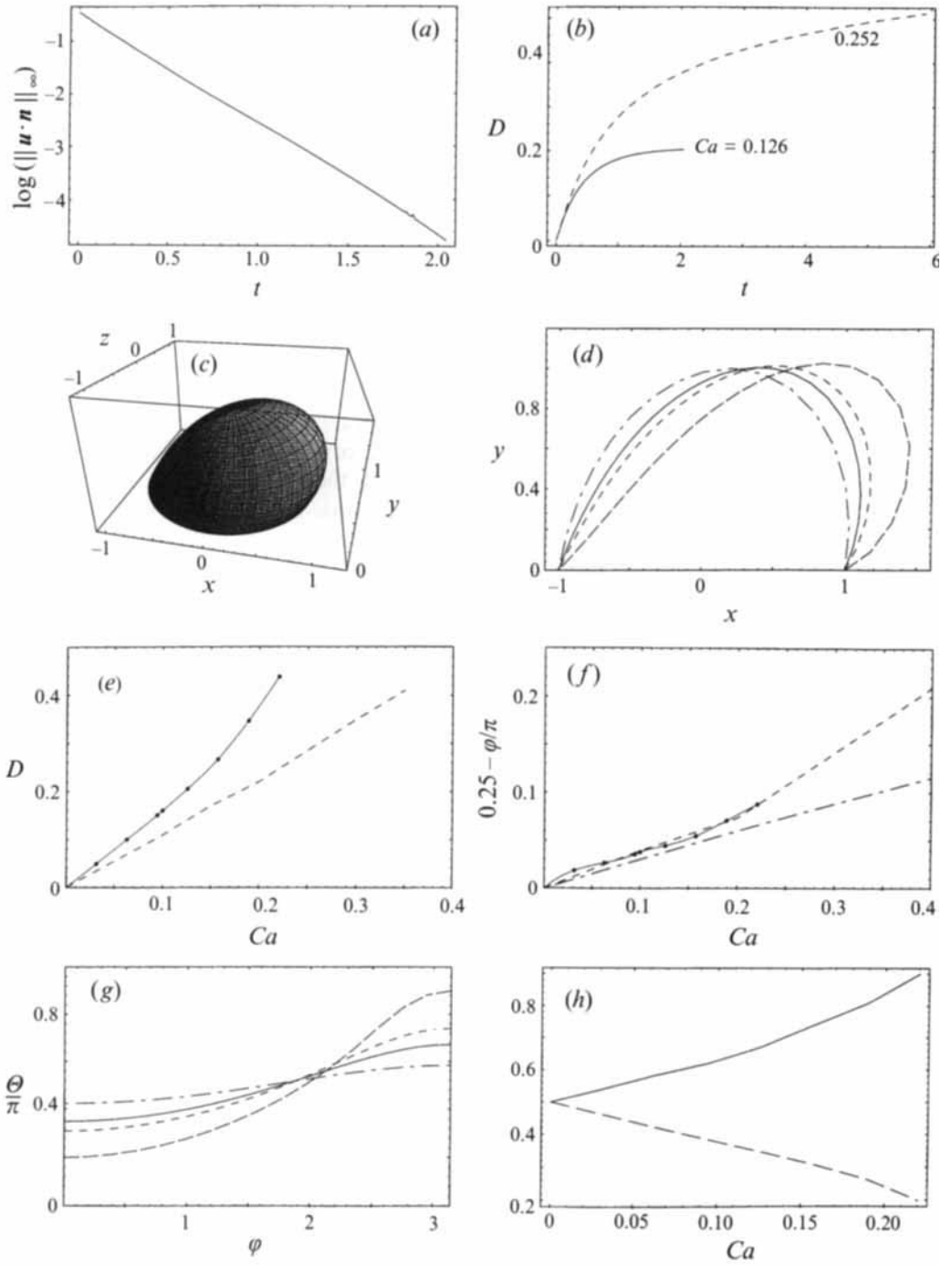

FIGURE 6. Shear flow past a drop with hemispherical shape at different capillary numbers. (*a*) The evolution of the maximum magnitude of the normal velocity at the interface for $Ca = 0.126$, shown by plotting $\log(\|u \cdot n\|_\infty)$ as function of time. (*b*) The evolution of the deformation parameter D. (*c*) Asymptotic drop shape for $Ca = 0.126$. (*d*) Cross-section of steady deformed drops in the (x, y)-plane for: —·—, $Ca = 0.063$; ——, $Ca = 0.126$; – – –, $Ca = 0.157$; ————, $Ca = 0.22$. (*e*) The deformation parameter D as a function of Ca: ——, the present study; – – –, Kennedy *et al.* (1994) for unbounded shear flow. (*f*) Variation of the inclination angle ϕ as function of Ca: ——, present study; – – –, Kennedy *et al.* (1994); —·—, Cox (1969). (*g*) Same as (*d*) but for the contact angle Θ/π plotted as a function of the azimuthal angle φ. (*h*) Advancing (——) and receding contact angles (– – –) as functions of the capillary number.

at larger deformations, the curve $D(Ca)$ becomes concave upwards, and its shape is similar to that of the analogous curve for drops suspended in an *infinite* shear flow, shown with the dashed line in figure 6(*e*) after Kennedy *et al.* (1994).

It is instructive to compare the behaviour of the function $D(Ca)$ at small capillary numbers with that reported by Feng & Basaran (1994) for a two-dimensional inviscid bubble protruding from a slot. They find that the slope of the $D(Ca)$ curve at small deformations is the same as that occurring in the absence of the wall. An explanation lies in the fact that the solution for infinite shear flow past a circular bubble also satisfies the no-slip condition at the mid-plane $y = 0$ which may therefore be regarded as a wall. This is also true for a spherical inviscid bubble suspended in *infinite* shear flow, but not for a drop with finite viscosity (Bartok & Mason 1958): the motion within a drop causes the onset of a finite velocity in the y-direction at the $y = 0$ plane associated with the presence of closed streamlines. The solution for shear flow over a hemispherical rigid protuberance on a plane wall, representing an attached drop of very large viscosity, is available in terms of an infinite expansion (Price 1985), but the complexity of the analysis renders the analogous computation for a liquid drop an arduous task that lies outside the scope of the present work.

In figure 6(*f*) we plot with dots the polar angle corresponding to the maximum radial distance of the interface from the origin in the (x, y)-plane with respect to the capillary number. The dashed line shows the inclination angle of a drop that is suspended in infinite shear flow after Kennedy *et al.* (1994), and the dot-dashed shows the predictions of a corresponding asymptotic theory for small deformations due to Cox (1969). As in the case of unbounded flow, as Ca is increased the inclination angle decreases monotonically from the initial value of $\pi/4$ corresponding to the principal direction of the rate-of-deformation tensor of the incident shear flow, which means that the drop tends to lean towards the wall. The inclination angle in the presence of the wall is remarkably close to that for infinite shear flow. The predictions of the asymptotic theory are accurate only in a limited range of small deformations.

The numerical computations have shown that there is a critical value of the capillary number below which the drop elongates and reaches a steady state, and above which it continues to elongate until the numerical method is no longer able to describe the motion with sufficient accuracy and reasonable computational cost. The behaviour of the deformation parameter D for a case where a steady asymptotic shape is not established is shown with a dashed line in figure 6(*b*). The numerical results place the critical value Ca_{cr} somewhere between 0.22 and 0.25. Noting that the corresponding critical capillary number for infinite shear flow is equal to 0.37 (Kennedy *et al.* 1994) suggests once more that the presence of the wall promotes the deformation and undermines the integrity of a drop.

The continued elongation of a drop with $Ca = 0.252$ is illustrated in figure 7(*a–e*). At long times, the rear portion of the drop is pushed downwards toward the wall and develops a region of negative curvature, whereas the front of the drop shows a tendency to roll over the wall. To demonstrate this behaviour more clearly, in figure 7(*f*) we plot the contour of the interface in the (x,y)-plane at a sequence of characteristic times. On the basis of the depicted shapes, one may speculate that, at long times, the drop will break up into two fragments, one of which will remain attached to the wall. Preliminary stages of this motion are evident in the contorted shape shown in figure 7(*e*). From a numerical standpoint, it is interesting to note the significant regriding of the interface as the surface area of the drop becomes larger. The computations are terminated at the point where the curvilinear coordinates are no longer effective and the numerical error is not small.

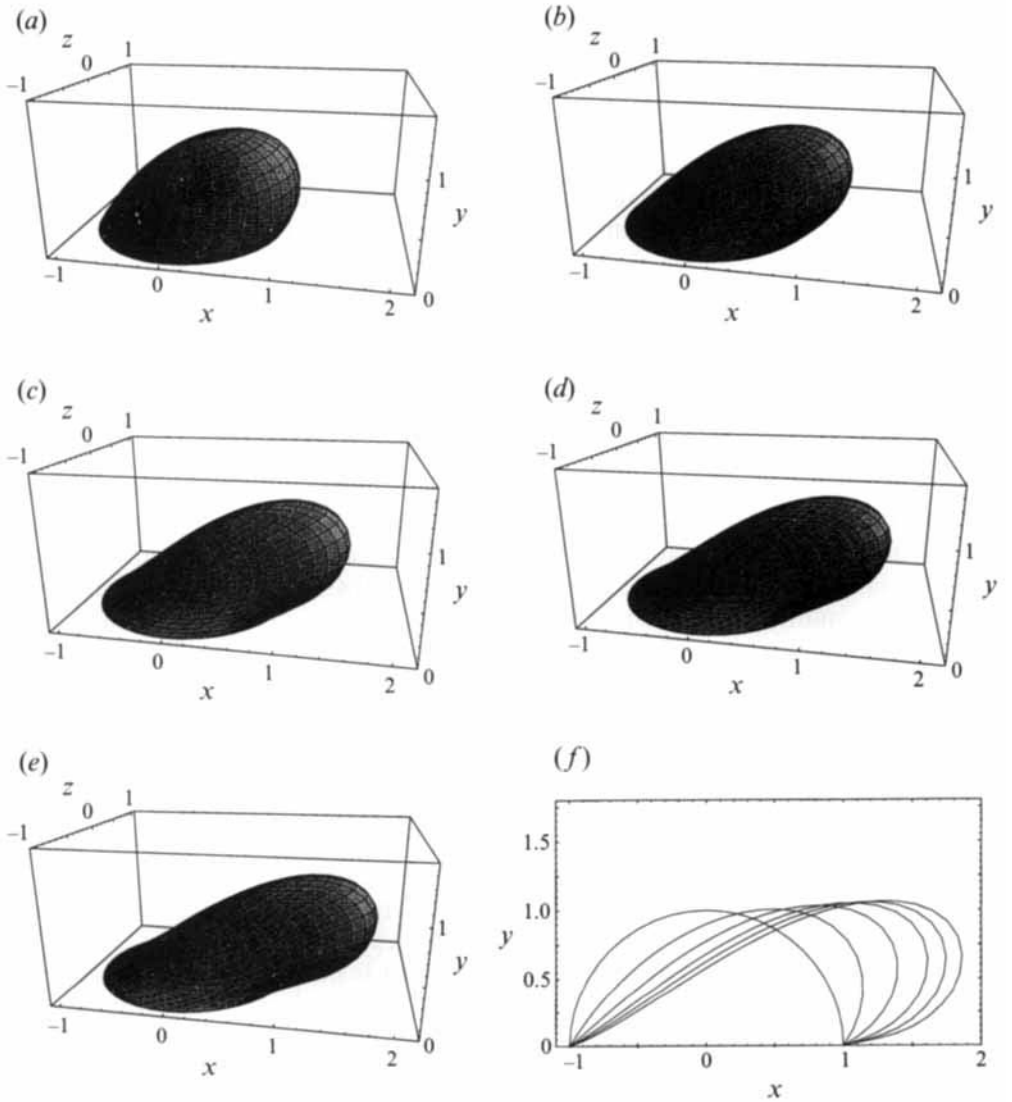

FIGURE 7. Evolution of an initially hemispherical drop for $Ca = 0.252$ at times (*a*) $kt = 0.822$, (*b*) 2.579, (*c*) 5.887, (*d*) 9.206, (*e*) 12.721. (*f*) The cross-sections of the drop in the (x, y)-plane at the times shown in (*a–e*).

The rate of decay of the normal component of the interfacial velocity δ defined at the beginning of this section is a measure of the time it takes a drop to reach a steady state. The numerical results show that $\delta = 9.76k$ at $Ca = 0.0315$, $\delta = 4.53k$ at $Ca = 0.063$, $\delta = 3.08k$ at $Ca = 0.0945$, and $\delta = 2.06k$ at $Ca = 0.126$. The larger the capillary number, the smaller the value of δ, and the longer it takes a drop to reach equilibrium; at the critical value Ca_{cr}, δ vanishes and the required time becomes infinite.

4.1.2. *Distribution of the contact angle*

Concentrating on the motion at capillary numbers that are lower than the critical value for steady deformation, we examine the distribution of the contact angle around

$c/b \setminus a/l$	0.622	0.794	1.091
0.5	0.165 ± 0.015	0.143 ± 0.016	0.113 ± 0.013
1	0.2 ± 0.018	0.236 ± 0.016	0.191 ± 0.027
2	0.235 ± 0.015	0.219 ± 0.019	0.135 ± 0.015

TABLE 2. Critical capillary number Ca_{cr}, where l is equal to the maximum dimension of the base.

the contact line. In figure 6(*g*) we plot the distribution of the contact angle as a function of the azimuthal angle φ measured around the y-axis from the negative x-axis, for $Ca = 0.063, 0.126, 0.157$ and 0.22. In the hydrostatic state the distribution of Θ is uniform, equal to $\pi/2$, but in the asymptotic deformed state we observe substantial variations. For instance, the variation for $Ca = 0.126$ amounts to 65% of the hydrostatic value. In all cases, the contact angle increases from the far upstream point to the far downstream point, with maximum and minimum contact angles occurring in the (x,y)-plane. If the contact angle at a particular point were to cross the thresholds defined by contact-angle hysteresis, the contact line would rearrange itself in order to eliminate this occurrence, obtaining an elongated shape.

As the capillary number is increased, the distribution of the contact angle becomes wider and tends to exhibit sharper variations of larger amplitude at the downstream rather than the upstream portion of the drop. Furthermore, the contact angle obtains the hydrostatic value $\pi/2$ at a point that is located further downstream from the centre of the circular base. Physically, this behaviour suggests that the front of the drop is likely to start moving before the rear when the contact angle exits the hysteresis window enclosed by Θ_A and Θ_R. To establish the critical capillary number above which the distribution of the contact line moves outside the hysteresis window, in figure 6(*h*) we plot the maximum and minimum values of the contact angle against Ca, as deduced from the numerical computations. As Ca approaches the critical value for continued deformation, Θ_{min} tends to vanish whereas Θ_{max} tends to become equal to π, which indicates that both the far upstream and downstream portions of the drop tend to become tangential to the wall. Based on these observations one may speculate that a hemispherical drop will begin sliding before it elongates and disintegrates under the action of the simple shear flow.

4.2. *Effect of drop volume*

The behaviour of drops whose volume is smaller or larger than that corresponding to the hydrostatic hemispherical shape is similar to that discussed in the preceding subsection. Note that as the ratio a/b becomes very large, the drop tends to obtain the hydrostatic shape of a whole sphere in point contact with the wall. In all cases we find that there is a critical capillary number defined with respect to the maximum height of a drop in the hydrostatic state, shown in table 2, above which the drop is unable to reach a steady shape and exhibits continued deformation. The value of this critical capillary number ranges between 0.252 and 0.164, and is thus a rather weak function of the drop volume. This range is substantially lower than the critical value predicted on the basis of the results for a drop that is immersed in an *infinite* unbounded shear flow; for a whole spherical drop in point contact with the wall, the later is equal to 0.74 (Kennedy *et al.* 1994). These significant differences underline once more the destabilizing influence of the wall.

Above the critical capillary number, the drops exhibit continued elongation possibly leading to breakup. An example of a continued elongation of a drop with $a/b = 2.609$

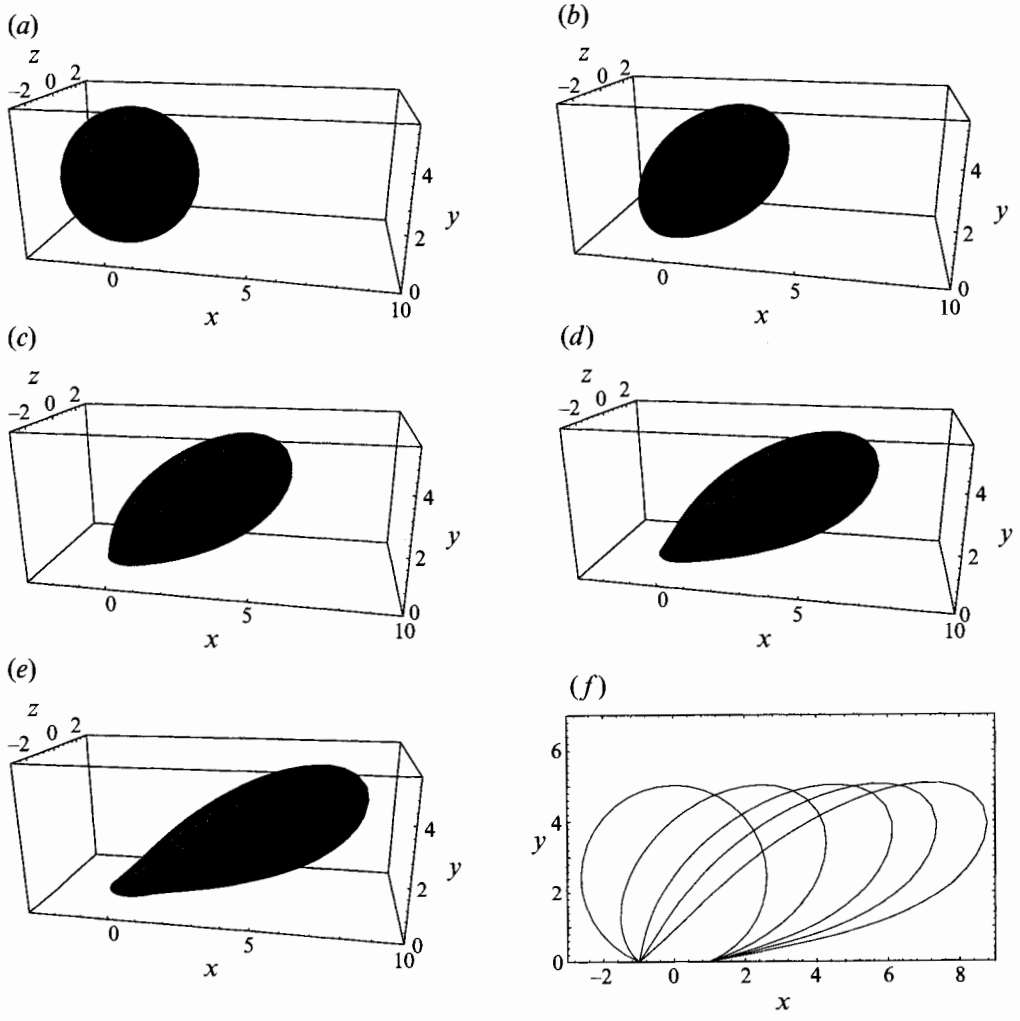

FIGURE 8. Sequence of evolving drop shapes for $a/b = 2.609$ and $Ca = 0.578$ at times (*a*) $kt = 0$, (*b*) 0.599, (*c*) 1.263, (*d*) 1.728, (*e*) 2.275. (*f*) The cross-sections of the drop in the (x, y)-plane at the times shown in (*a–e*).

at $Ca = 0.578$, whose volume is larger than that corresponding to the hemisphere, is shown in figure 8(*a–f*). The tendency of the drop to detach is evident in the thinning of the cross-sectional area around the base shown in figure 8(*f*). An example of a continued elongation of a drop with $a/b = 0.622$ at $Ca = 0.291$ whose volume is smaller than that corresponding to the hemisphere, is shown in figure 9(*a–f*). The tendency of the drop to detach is evident in the interfacial corrugations around the base shown in figure 9(*f*).

It is instructive to consider changes in the drop behaviour on maintaining the value of Ca fixed and varying the drop volume. In figure 10(*a*, *b*) we present asymptotic steady shapes of drops with equivalent radii $a/b = 0.622$ and 1.091 for capillary number $Ca = 0.126$. The shape of a drop for $a/b = 0.794$, corresponding to a hemispherical hydrostatic shape, was illustrated in figure 6(*c*). It is evident that, as the volume of the drop is reduced, its rear portion tends to flatten and eventually develops a region of negative curvature in the (x,y)-plane; roughly speaking, the drop

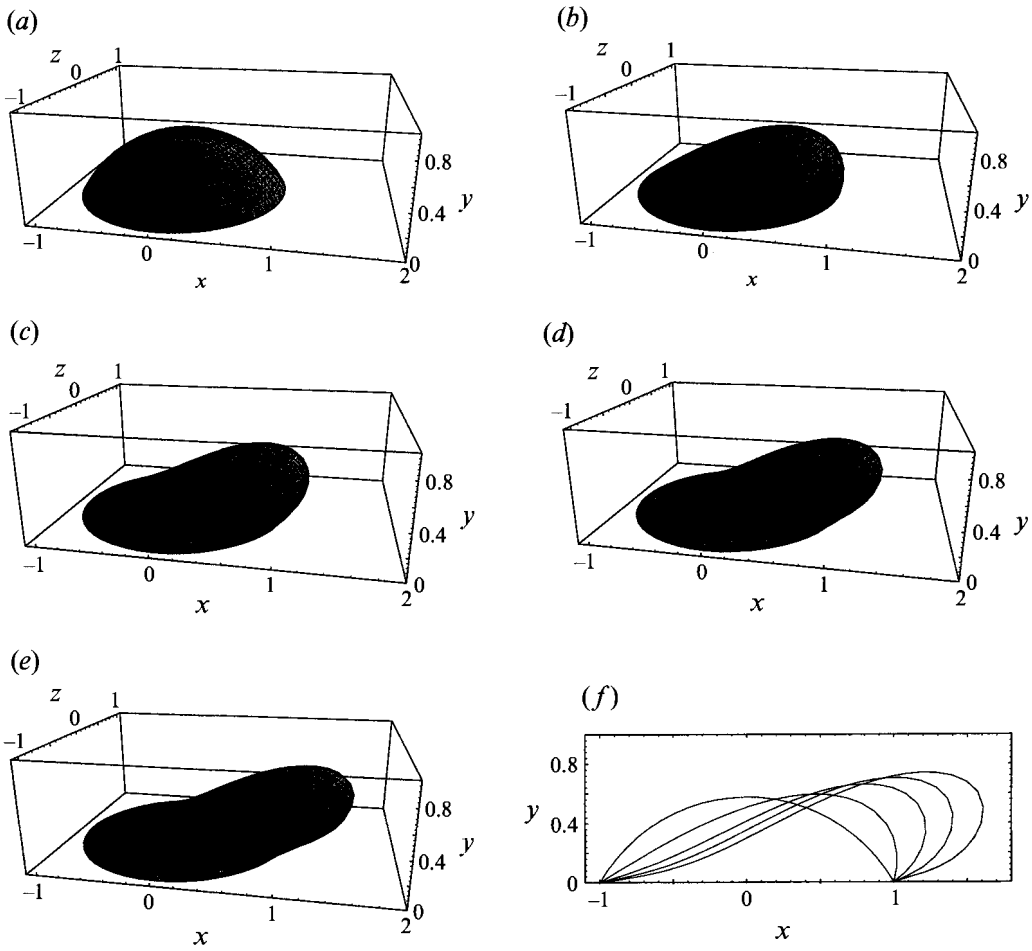

FIGURE 9. Sequence of evolving drop shapes for $a/b = 0.622$ and $Ca = 0.291$ at times (*a*) $kt = 0$, (*b*) 1.182, (*c*) 3.396, (*d*) 5.529, (*e*) 7.706. (*f*) The cross-sections of the drop in the (x, y)-plane at the times shown in (*a–e*).

is pressed down by the incident flow. In all cases, the front portion of the drop projects into the flow.

In figure 10(*c*) we plot the corresponding distributions of the contact angle along the contact line. Figure 10(*d*) is identical to figure 10(*c*) except that the contact angle is shifted by the uniform contact angle of the hydrostatic shape. The curves corresponding to the small and large volumes exhibit the strongest variations and nearly the same range of variation between Θ_{min} and Θ_{max}. This indicates that the contact lines of drops with small or large volumes are likely to move before those of drops with the intermediate volumes.

When both a/b and Ca are sufficiently small, the drop obtains a flat shape, and the motion of the fluid within the drop may be described on the basis of the theory of lubrication flow (Dussan V. 1987). Two important assumptions of this theory are that the disturbance flow around the drop is decoupled from the locally unidirectional parabolic flow inside the drop, and the flow inside the drop is driven primarily by the shear stress due to the incident simple shear flow, $\boldsymbol{u}^{\infty} = (ky, 0, 0)$. The capillary pressure field due to variations of the mean curvature makes an additional contribution to the

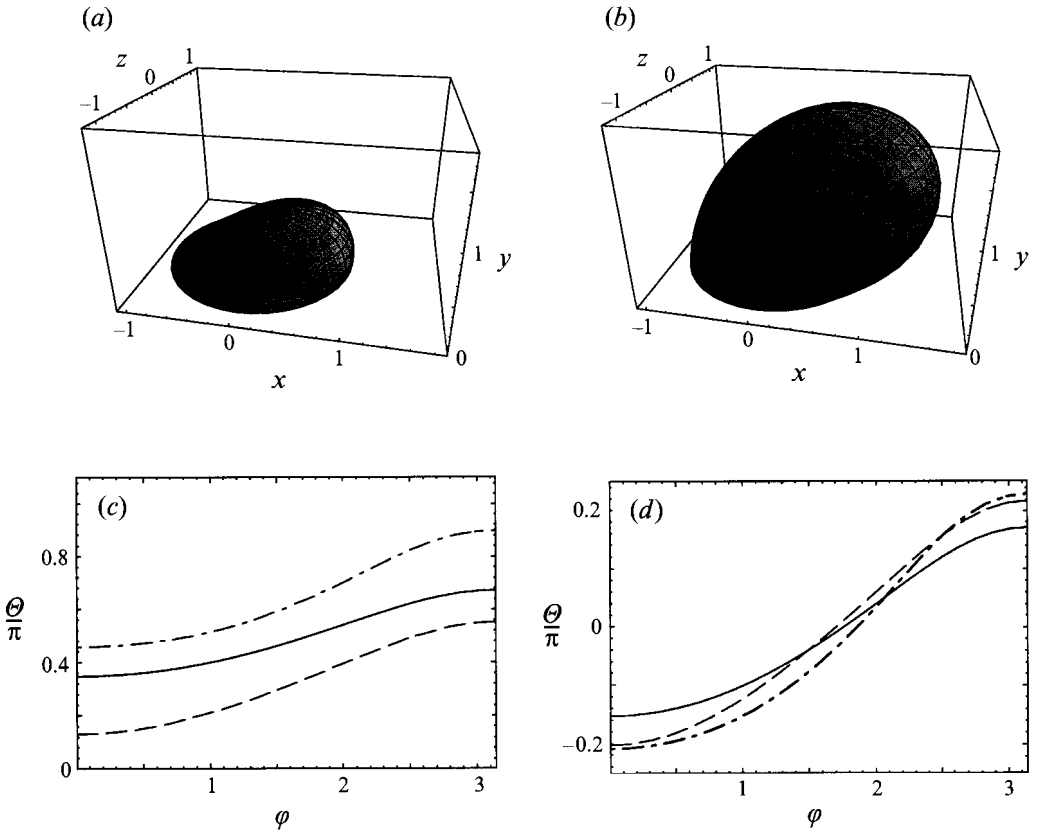

FIGURE 10. The effect of drop volume for a fixed capillary number $Ca = 0.126$. (*a,b*) Steady drop shape for (*a*) $a/b = 0.622$; (*b*) $a/b = 1.091$. (*c*) Contact angle distribution: ———, $a/b = 0.622$; ——, $a/b = 0.794$; — - —, $a/b = 1.091$. (*d*) Same as (*c*) but shifted by the initial uniform contact angle to show relative variations.

momentum balance. The boundary conditions on the two components of the velocity that are tangential to the wall inside the drop are

$$\frac{\partial u_x}{\partial y} = k \quad \text{and} \quad \frac{\partial u_z}{\partial y} = 0, \quad \text{at the drop surface} \quad y = h(x,z). \tag{4.1}$$

To establish the range of validity of the lubrication theory, we consider the flow past a drop with equivalent radius $a/b = 0.423$ at $Ca = 0.02$. In figure 11(*a*) we show the deformed steady shape established at large times; the ratio between the maximum drop height and radius of the contact line is $h_{max}/b = 0.230$, which is moderately but not exceedingly small. In figure 11(*b*, *c*) we present profiles of the x and z velocity components across the height of the drop at three randomly selected points shown with dots in figure 11(*a*). The dots in figure 11(*b*, *c*) indicate the position of the interface. We observe that all profiles have a parabolic shape inside the drop, and the profile of u_x becomes almost linear above the drop. The negative velocities in figure 11(*b*) reveal the presence of recirculating flow inside the drop. The slopes of the profiles at the interface are in good agreement with the boundary conditions stated in (4.1). These observations validate the assumptions of lubrication flow even for drops with moderate height, and corroborate the use of approximate models for the analysis of flow over stationary or even sliding drops.

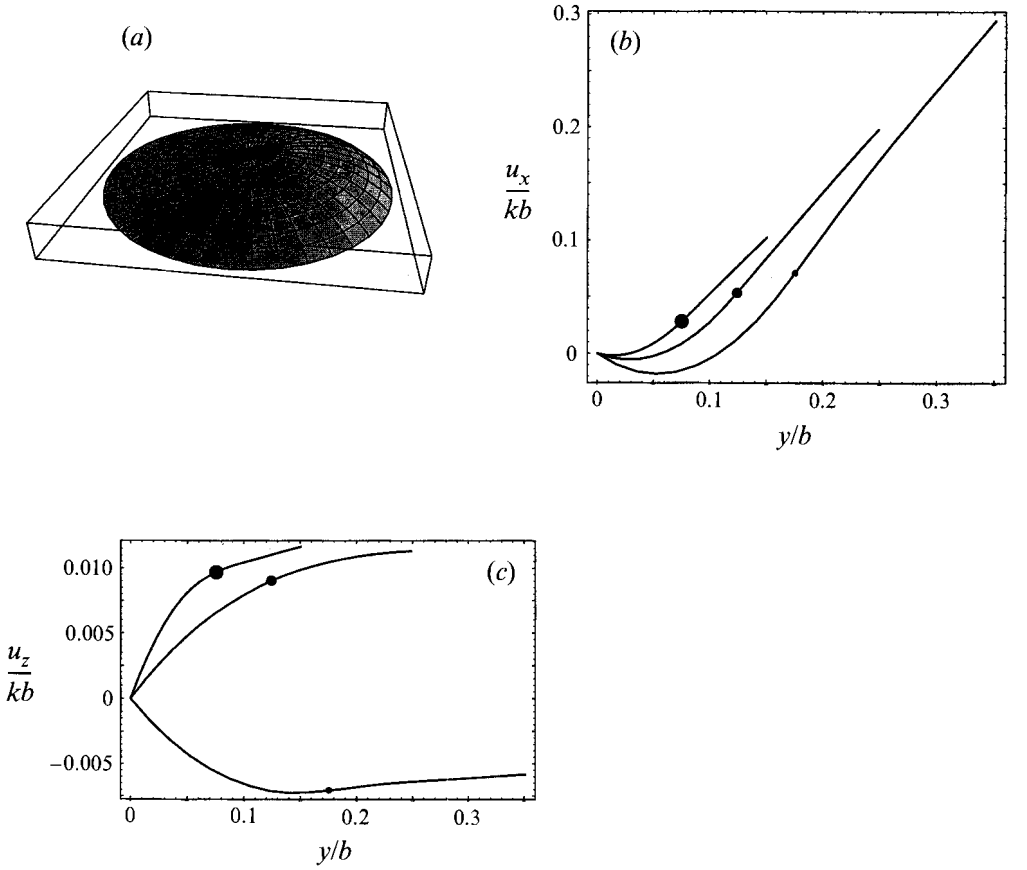

FIGURE 11. Behaviour of flat drops and validation of the assumptions of lubrication theory. (*a*) Steady deformed shape of a flat drop $a/b = 0.423$ with circular contact line for $Ca = 0.02$. (*b*) Profile of the x-velocity component across the drop at three randomly selected points shown with dots in (*a*). (*c*) Same as (*b*) but for the z-velocity component. The dots in (*b*) and (*c*) indicate the position of the interface.

5. Deformation of drops with elliptical contact lines

Results for drops with elliptical contact lines revealed behaviour that is qualitatively similar to that described in §4 for drops with circular contact lines. We find that there exists a critical value of the capillary number Ca_{cr}, above which a drop deforms continuously under the influence of the incident flow, and another critical capillary number above which the contact-angle distribution is likely to exit the hysteresis window. The latter, however, cannot be computed before the values of the receding and advancing contact angles are specified.

In table 2 we present estimates of Ca_{cr} for three values of the aspect ratio of the elliptic contact line $c/b = 0.5, 1, 2$ and three values of the reduced equivalent drop radius a/l, where l is the maximum dimension of the base, $l = \max(b, c)$. When $c/b = 0.5$ the major axis of the ellipse is positioned in the direction of the shear flow, whereas when $c/b = 2$ it is positioned in a transverse manner with respect to the shear flow. Maintaining the conventions of §4, we define the capillary number with respect to the maximum drop height in the hydrostatic state.

The results of table 2 indicate that the critical capillary number ranges between 0.10

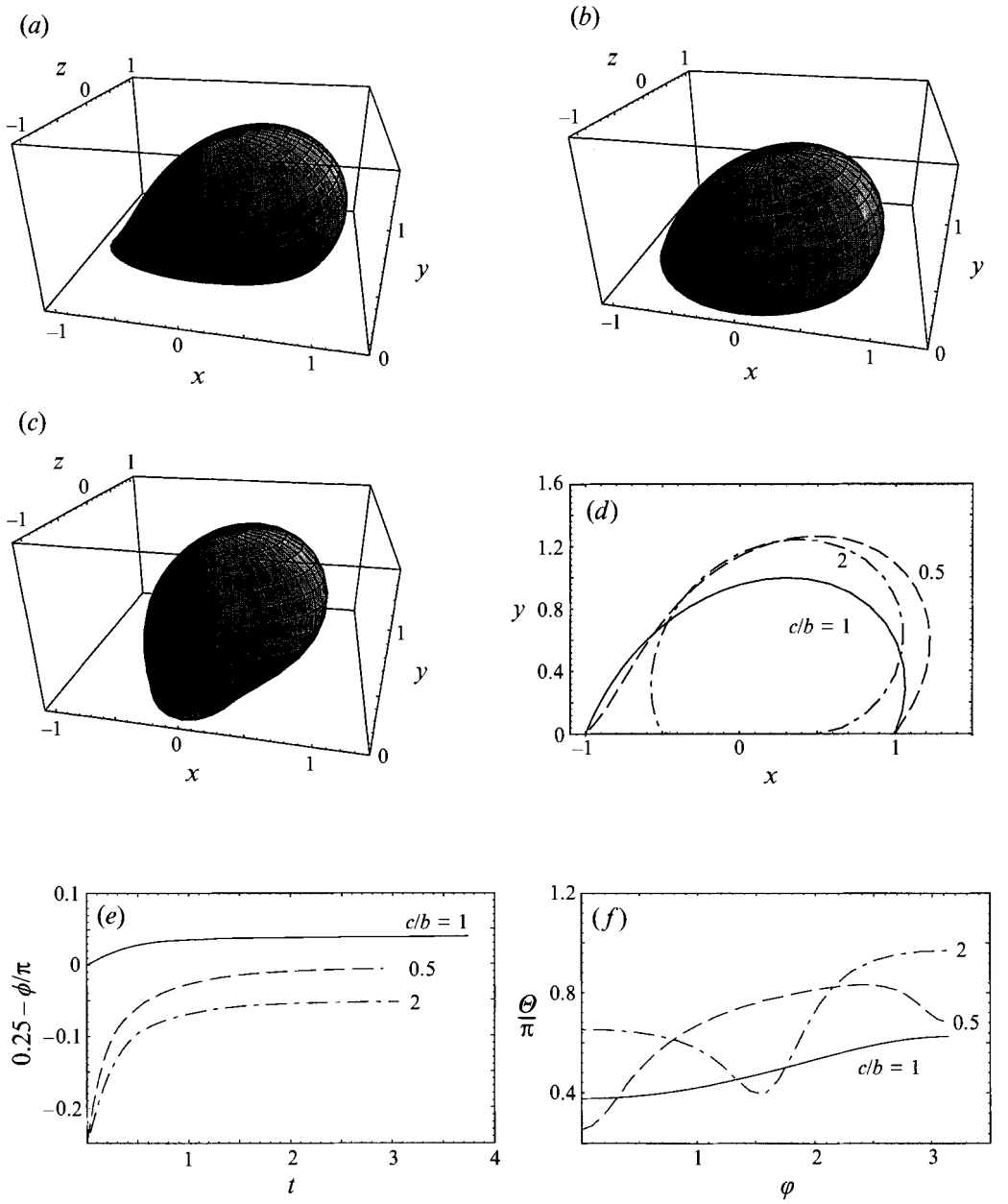

FIGURE 12. The effect of aspect ratio of the contact line for fixed equivalent drop radius $a/l = 0.794$ and capillary number $Ca = 0.1$. (*a–c*) Steady deformed drop shape with contact-line aspect ratio (*a*) $c/b = 0.5$; (*b*) $c/b = 1$; (*c*) $c/b = 2$. (*d*) Drop contours in the (x, y)-plane. (*e*) Evolution of drop inclination. (*f*) Contact-angle distribution: ———, $c/b = 0.5$; ——, $c/b = 1$; —·—, $c/b = 2$.

and 0.24; this relatively mild variation corroborates the choice of the drop height as the appropriate length scale in the definition of the capillary number. It is interesting to note that the critical value of the capillary number increases monotonically down the first column corresponding to small drops, but obtains a maximum value at the middle entries of the second and third columns corresponding to drops with moderate and large size. On the other hand, the critical value of the capillary number decreases

monotonically across the first and third rows corresponding to eccentric contact lines, but obtains a moderate maximum value at the middle entry of the second row corresponding to drops with circular contact lines. These differences underline the importance of the geometry of the contact line not only for the hydrostatic shape, but also for the nature of the transient and asymptotic deformation.

To illustrate the effect of aspect ratio of the contact line on the shape of steadily deformed drops, in figure 12(*a–c*) we present the steady shapes of drops for $c/b = 0.5, 1, 2$ all with $a/l = 0.794$ corresponding to a hemispherical hydrostatic drop with a circular contact line, for capillary number $Ca = 0.10$. The critical values of the capillary number are listed in the second column of table 2. For $c/b = 0.5$ the computations start from the hydrostatic shape shown in figure 3(*b*), whereas for $c/b = 2$ the initial shape is obtained by rotating the shape shown in figure 3(*b*) by 90° around the y-axis. Comparing the steady shape shown in figure 12(*b*) for a circular contact line, to those shown in figure 12(*a, c*) for eccentric contact lines, we find that the latter are appreciably more involved. The effect of the contact line eccentricity on the asymptotic shape is illustrated more directly in figure 12(*d*) where we plot the drop contours in the (x, y)-plane.

To illustrate the effect of the contact line on drop inclination, in figure 12(*e*) we plot the evolution of the polar angle corresponding to the maximum radial distance of the interface from the origin in the (x, y)-plane. It is interesting to note that the initial inclination is equal to $\pi/4$ for the circular contact line, and $\pi/2$ for the eccentric contact lines. In the asymptotic state, the drop with the circular contact line is tilted towards the wall more than the drops with the elliptical contact lines. The significance of the inclination angle, however, is diminished by the fact that the interfaces obtain convoluted shapes.

The effect of the contact-line eccentricity is further demonstrated by examining the distribution of the contact angle shown in figure 12(*f*). Concentrating on the case $c/b = 0.5$, we compare the contact-angle distribution in the deformed state, shown with a dashed line in figure 12(*f*), to that in the hydrostatic state shown with a dash-dotted line in figure 3(*f*), and find that the position of maximum angle is shifted downstream, and its value is increased by a small amount. Furthermore, the magnitude of the minimum contact angle has decreased substantially with respect to that in the hydrostatic state. For $c/b = 2$, similar comparisons reveal that the positions of maximum and minimum contact angle are virtually unaffected by the motion, the magnitude of the maximum contact angle increases substantially, whereas the magnitude of the minimum contact angle is only sightly perturbed. These observations suggest that drops with non-circular contact lines are likely to slide over the wall before drops with circular contact lines.

This research was supported by the National Science Foundation Grant under grant CTS-9216176, and the Department of Energy. Partial support was provided by the Exxon Education Foundation. Computing time was provided by the San Diego Supercomputer Center.

REFERENCES

ABRAMOWITZ, M. & STEGUN, I. A. 1970 *Handbook of Mathematical Functions*, p. 883. Dover.

BARTOK, W. & MASON, S. G. 1958 Particle motions in sheared suspensions. VII. Internal circulation in fluid droplets (theoretical). *J. Colloid Sci.* **13**, 293–307.

BEAR, J. 1972 *Dynamics of Fluids in Porous Media*. Dover.

Cox, R. G. 1969 The deformation of a drop in a general time-dependent fluid flow. *J. Fluid Mech.* **37**, 601–623.

Durbin, P. A. 1988*a* Free-streamline analysis of deformation and dislodging by wind force of drops on a surface *Phys. Fluids* **31**, 43–48.

Durbin, P. A. 1988*b* On the wind force needed to dislodge a drop adhered to a surface. *J. Fluid Mech.* **196**, 205–222.

Dussan V., E. B. 1979 On the spreading of liquids on solid surfaces: static and dynamic contact lines. *Ann. Rev. Fluid Mech.* **11**, 371–400.

Dussan V., E. B. 1985 On the ability of drops or bubbles to stick to non-horizontal surfaces of solids. Part 2. Small drops or bubbles having contact angles of arbitrary size. *J. Fluid Mech.* **151**, 1–20.

Dussan V., E. B. 1987 On the ability of drops to stick to surfaces of solids. Part 3. The influences of the motion of the surrounding fluid on dislodging drops. *J. Fluid Mech.* **174**, 381–397.

Dussan V., E. B. & Chow, R. T.-P. 1983 On the ability of drops or bubbles to stick to non-horizontal surfaces of solids. *J. Fluid Mech.* **137**, 1–29.

Feng, J. Q. & Basaran, O. A. 1994 Shear flow over a translationally symmetric cylindrical bubble pinned on a slot in a plane wall. *J. Fluid Mech.* **275**, 351–378.

Furmidge, C. G. L. 1962 Studies at phase interfaces. I. The sliding of liquid drops on solid surfaces and a theory for spray retention. *J. Colloid Sci.* **17**, 309.

Haley, P. J. & Miksis, M. J. 1991 The effect of the contact line on droplet spreading. *J. Fluid Mech.* **223**, 57–81.

Hornung, U. & Mittelmann, H. D. 1990 A finite element method for capillary surfaces with volume constraints. *J. Comput. Phys.* **87**, 126–136.

Kennedy, M. R., Pozrikidis, C. & Skalak, R. 1994 Motion and deformation of liquid drops and the rheology of dilute emulsions in simple shear flow. *Computers Fluids* **23**, 251–278.

Lipowsky, H. H., Riedel D. & Shi, G. S. 1991 In vivo mechanical properties of leukocytes during adhesion venular endothelium. *Biorheology* **28**, 53–64.

Marmur, A. 1994 Contact angle hysteresis on heterogeneous smooth surfaces. *J. Colloid Interface Sci.* **168**, 40–46.

Milinazzo, F. & Shinbrot, M. 1988 A numerical study of a drop on a vertical wall. *J. Colloid Interface Sci.* **121**, 254–264.

Pozrikidis, C. 1992 *Boundary Integral and Singularity Methods for Linearized Viscous Flow*. Cambridge University Press.

Pozrikidis, C. 1993 On the transient motion of ordered suspensions of liquid drops. *J. Fluid Mech.* **246**, 301–320.

Pozrikidis, C. 1995*a* Finite deformation of liquid capsules enclosed by elastic membranes in simple shear flow. *J. Fluid Mech.* **297**, 123–152.

Pozrikidis, C. 1995*b* *Introduction to Theoretical and Computational Fluid Dynamics*. Oxford University Press.

Pozrikidis, C. 1995*c* Shear flow over an axisymmetric protuberance on a plane wall. *J. Engng Maths* (Submitted).

Press, W. H., Flannery, B. P., Teulosk, S. A. & Vetterling, W. T. 1992 *Numerical Recipes in C: the Art of Scientific Computing*. Cambridge University Press.

Price, T. C. 1985 Slow linear shear flow past a hemispherical bump in a plane wall. *Q. J. Mech. Appl. Math.* **38**, 93–104.

Stone, H. 1994 Dynamics of drop deformation and breakup in viscous fluids. *Ann. Rev. Fluid Mech.* **26**, 65–102.

Taylor, G. I. 1932 The viscosity of a fluid containing small drops of another fluid. *Proc. R. Roc. Lond.* A **138**, 41–48.

Zienkiewicz, O. C., & Taylor, R. L. 1989 *The Finite Element Method. Volume 1: Basic Formulation and Linear Problems*. McGraw-Hill.